JOURNAL OF GEOPHYSICAL RESEARCH, VOL. 108, NO. D20, 4643, doi:10.1029/2001JD001504, 2003

Temporal and spatial patterns of the interannual variability of total ozone in the tropics

Charles D. Camp
Department of Applied Mathematics, California Institute of Technology, Pasadena, California, USA

Mark S. Roulston
Pembroke College, Oxford, UK

Yuk L. Yung
Division of Geological and Planetary Sciences, California Institute of Technology, Pasadena, California, USA

Received 25 October 2001; revised 29 July 2002; accepted 20 December 2002; published 25 October 2003.

[1] The recently constructed gridded Merged Ozone Data (MOD) set, combining the monthly mean column abundances collected by the Total Ozone Mapping Spectrometer (TOMS) and the Solar Backscatter Ultraviolet (SBUV and SBUV/2) instruments, provides a nearly continuous record from late 1978 to 2000 on a $5^\circ \times 10^\circ$ latitude-longitude grid. The precision of these measurements and their calibration allow very small signals, $\sim$1% of total column ozone, to be clearly seen. Using MOD, we have carried out an empirical orthogonal function (EOF) study of the temporal and spatial patterns of the interannual variability of total column ozone in the tropics. The first four EOFs of our study capture over 93% of the variance of the deseasonalized data. The leading two EOFs of our study, respectively accounting for 42% and 33% of the variance, display structures attributable to the quasi-biennial oscillation (QBO), with influence from a decadal oscillation. The third EOF (15% of the variance) represents an interaction between the QBO and an annual cycle. The fourth EOF (3% of the variance) is related to the El Niño - Southern Oscillation. This EOF decomposition is robust; nearly identical patterns occur in the decomposition of various equatorial latitude bands of MOD and similar patterns occur in the analysis of the deseasonalized TOMS data set, a shorter record with a more finely resolved spatial grid. For comparison, similar decompositions were performed for dynamical fields from the reanalysis product from the National Centers for Environmental Prediction and the National Center for Atmospheric Research. Using these analyses, we found possible connections between the deduced patterns in ozone and the climate variables. *INDEX TERMS:* 0341 Atmospheric Composition and Structure: Middle atmosphere—constituent transport and chemistry (3334); 1610 Global Change: Atmosphere (0315, 0325); 1620 Global Change: Climate dynamics (3309); 3334 Meteorology and Atmospheric Dynamics: Middle atmosphere dynamics (0341, 0342); 3362 Meteorology and Atmospheric Dynamics: Stratosphere/troposphere interactions

Citation: Camp, C. D., M. S. Roulston, and Y. L. Yung, Temporal and spatial patterns of the interannual variability of total ozone in the tropics, *J. Geophys. Res.*, *108*(D20), 4643, doi:10.1029/2001JD001504, 2003.

1. Introduction

[2] The total column abundance of ozone in the atmosphere represents an intricate interaction between chemical and dynamical processes (see, for example, *Brasseur et al.* [1999]). A primary motivation for studying the interannual variability (IAV) of total ozone is to separate the anthropogenic perturbations of the ozone layer from natural variability (see, for example, *World Meteorological Organization* (*WMO*) [1999]). The latter imposes "noise" on the system that makes the detection of ozone depletion and its attribution to anthropogenic forcing more difficult. In addition, the IAV offers insights into the subtle coupling between chemistry and dynamics that are both important for determining the abundance and distribution of ozone, as well as providing opportunities to test the sensitivity of models to external and internal forcing.

[3] An extensive global data set is currently available for studying IAV of ozone. The Total Ozone Mapping Spectrometer (TOMS) instrument on the Nimbus 7 spacecraft measured the spatial distribution of total ozone from 1978 until 1993 [*Herman et al.*, 1991]. By scanning across the track of the satellite, TOMS obtained data between successive satellite orbital tracks. Daily TOMS gridded ozone data of Version 7 [*McPeters et al.*, 1996] (on a $1^\circ \times 1.25^\circ$ grid

0148-0227/03/2001JD001504

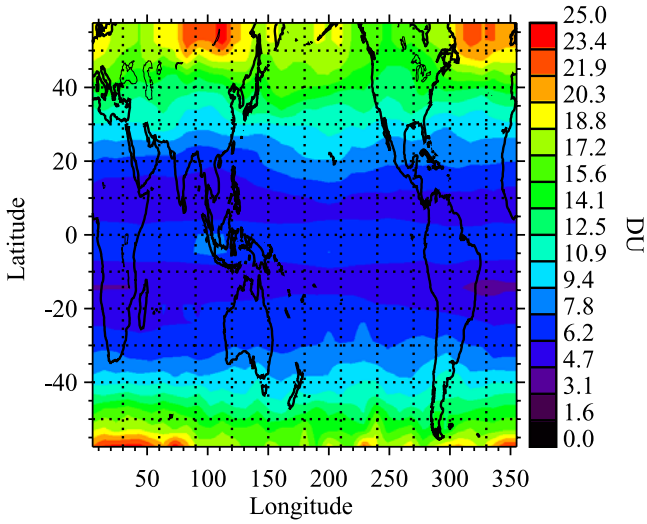

Figure 1. Standard deviations of the detrended, deseasonalized ozone time series from the Merged Ozone Data set.

in latitude and longitude) are available from 1979 to 1992. The data were extended to 2000 (on a 5° × 10° grid) in the Merged Ozone Data set (MOD), which combines the monthly mean column abundances of the of TOMS instruments on Nimbus 7 and Earth Probe with additional data from the Solar Backscatter Ultraviolet (SBUV and SBUV/2) instruments on Nimbus 7, NOAA 9, NOAA 11 and NOAA 14.

[4] Previous studies have fruitfully mined the rich TOMS data set. Using globally averaged TOMS data, *Herman et al.* [1991] deduced the ozone depletion trend, quasi-biennial oscillation (QBO) and a possible 11-year solar cycle variation. Using zonally averaged TOMS data, *Tung and Yang* [1994a, 1994b] studied the propagation of QBO effects from the tropics to the mid-latitudes, and the interaction between the QBO and the annual cycle, giving rise to 20-month and 8.6-month oscillations. *Shiotani* [1992] studied the zonal variability of ozone in the tropics related to the El Niño-Southern Oscillation (ENSO) and *Kayano* [1997] carried out an empirical orthogonal function (EOF) study of the relation between total ozone and ENSO.

[5] However, we notice a curious omission of a *simultaneous* decomposition of the TOMS data to reveal all spatial and temporal patterns in the tropics. This paper attempts to fill this gap in our analysis of total ozone.

[6] The restriction to the tropics was chosen because the mid-latitudes demonstrate more variability than the tropics. Standard deviations for the time series at each grid point of the detrended, deseasonalized Merged Ozone Data are shown in Figure 1. (Details of this data set and its processing are described in the following section.) The inclusion of data from higher latitudes in the analysis would result in EOF patterns dominated by mid-latitude signals. Therefore the tropical patterns would be much harder to isolate and analyze.

[7] In Section 2, the data sets and indices used are described. In Section 3, the EOF technique is briefly discussed. The results of the EOF analysis of the ozone data are shown in Section 4. Comparisons of this analysis to physical processes are done in Section 5. In Section 6, the EOF analysis of the NCEP-NCAR data is shown and compared to the ozone results. Section 7 contains our conclusions and final remarks.

2. Data Sets and Indices

[8] For this study, we have used two data sets for monthly mean column ozone abundances: Nimbus 7 TOMS [*McPeters et al.*, 1996] and the Merged Ozone Data (MOD) as described in the NASA web-site, http://code916.gsfc.nasa.gov/Public/Analysis/merged (R. S. Stolarski, S. Hollandsworth, R. McPeters, L. Flynn, and G. Labow, manuscript in preparation, 2001). For both data sets, we have restricted our analysis to a tropical band from 25°S to 25°N. To lower the computational load of the EOF analysis, the TOMS data has been rebinned from its original 1° × 1.25° grid to a 2° × 7.5° grid. The MOD data is on a 5° × 10° grid. We have used the TOMS data from Nov., 1978 to Apr., 1993 and the MOD data from Nov., 1978 to Dec., 2000.

[9] Data from the National Centers for Environmental Prediction and National Center for Atmospheric Research (NCEP-NCAR) reanalysis were also analyzed [*Kalnay et al.*, 1996]. To match the analyses performed on the ozone data sets, we restricted the EOF analysis of the NCEP-NCAR fields to the 25°S to 25°N tropical band. The data were also rebinned from the original 2.5° × 2.5° grid to a 2° × 7.5° grid. Cubic spline interpolation was used to refine the latitude spacing. The EOF analysis was performed on data from Jan., 1979 to Sept., 1999.

[10] All data sets were detrended by removing the linear long-term trends from the time series of each grid point; the linear trends were determined by a least squares fit. Seasonal cycles for each time series were also removed; cycles were determined by taking averages for each month independently. Missing months were replaced by cubic spline interpolation in time. To isolate interannual variability from higher frequency oscillations, further filtering was performed spectrally. The spectral filter applied was a convolution of a step function with a Hanning window chosen to obtain a full signal from periods above 15 months and no signal from periods below 12.5 months; see *Press et al.* [1992]. The details of this filter, Lowpass A, and other similarly constructed filters used in this study are shown in Table 1.

[11] Various indices were used to help identify the processes seen in the EOF analyses. For a QBO index, we used the QBO Zonal Wind Index, 1953 - September 2001. For our

Table 1. Frequency Filters[a]

Filter Name	Period Ranges (months)	
	Passed	Stopped
Lowpass A	(15, max)	(0, 12.5)
Lowpass B	(40.5, max)	(0, 34.5)
Lowpass C	(72, max)	(0, 50)
Bandpass A	(15, 72)	(0, 12.5) and (96, max)
Bandpass B	(15, 34.5)	(0, 12.5) and (40.5, max)
Bandstop A	(0, 9.5) and (12.5, max)	(11.5, 12.5)

[a]Passed ranges correspond to frequencies unaltered by the spectral window. Stopped ranges correspond to frequencies completely blocked. Frequencies in the transition intervals are damped; the spectral windows used are convolutions of a Hanning window and a step function.

time interval, this index uses the 30 hPa zonal wind measured above Singapore (1°N, 104°E). Further details can be found in *Naujokat* [1986], *Marquardt* [1997] and *Marquardt and Naujokat* [1997]. For an ENSO index, we used the SOI: Standardized Sea Level Pressure Anomaly time series described in the International Research Institute for Climate Prediction (IRI) web site: http://ingrid.ldgo.columbia.edu/SOURCES/.Indices/.soi/.dataset_documentation.html. For a solar cycle index, we used the Adjusted Monthly Solar Flux: 2800 MHz Series C time series, described on the NOAA web site: http://spidr.ngdc.noaa.gov/spidr/help/solar_main.htm#flux. Linear detrending and lowpass filtering, using the Lowpass A filter, were performed on all indices.

[12] For presentation purposes only, the data for all color figures have been bilinearly interpolated to a much finer spatial resolution.

3. Methodology

[13] Given a multivariate data set consisting of measurements from S stations taken simultaneously at T times, the EOFs are found by determining the eigenvectors of the covariance matrix, $\mathbf{C}$, of the data set constructed from the T measurement vectors, $\mathbf{x}_t$ (i.e., the state of the system at time t) [*Preisendorfer*, 1988]. If $\mathbf{X}$ is the matrix given by $\mathbf{X} = [\mathbf{X}_t]^*$ $(T \times S)$ and the temporal means of the data from each station have been removed, then the covariance matrix is given by

$$\mathbf{C} = \frac{1}{T}\mathbf{X}^*\mathbf{X} \qquad (S \times S) \tag{1}$$

The covariance matrix is a real symmetric positive-semidefinite matrix and can therefore be written as

$$\mathbf{C} = \mathbf{Q}\mathbf{\Lambda}\mathbf{Q}^* \tag{2}$$

where $\mathbf{\Lambda}$ is a diagonal matrix whose elements are the S real, non-negative eigenvalues, λ, and $\mathbf{Q}$ is an orthogonal matrix whose columns are the S orthonormal eigenvectors, $\mathbf{e}$. These eigenvectors are the EOFs and form a new basis with which the original data can be represented,

$$\mathbf{X} = \mathbf{P}\mathbf{Q}^* = \sum \mathbf{p}\mathbf{e}^* \qquad (T \times S) \tag{3}$$

$\mathbf{P}$ is a $(T \times S)$ matrix whose columns, $\mathbf{p}$, are the S principal component time series (PCs) determined by projecting the original data set onto the associated EOFs,

$$\mathbf{p} = \mathbf{X}\mathbf{e} \tag{4}$$

Combining equations (1), (2) and (3), we can see that

$$\mathbf{\Lambda} = \frac{1}{T}\mathbf{P}^*\mathbf{P} \tag{5}$$

Since $\mathbf{\Lambda}$ is diagonal, the PCs ($\mathbf{p}$) are mutually orthogonal and the eigenvalues (λ) are equal to their variances. In the context of this study, the EOFs can be considered two-dimensional spatial standing waves while the associated PCs are the time-dependent amplitudes of their oscillations. The associated eigenvalues are the variances captured by each EOF. When sorted by decreasing λ, the leading n eigenvectors (EOFs) describe more variance than any other n vectors.

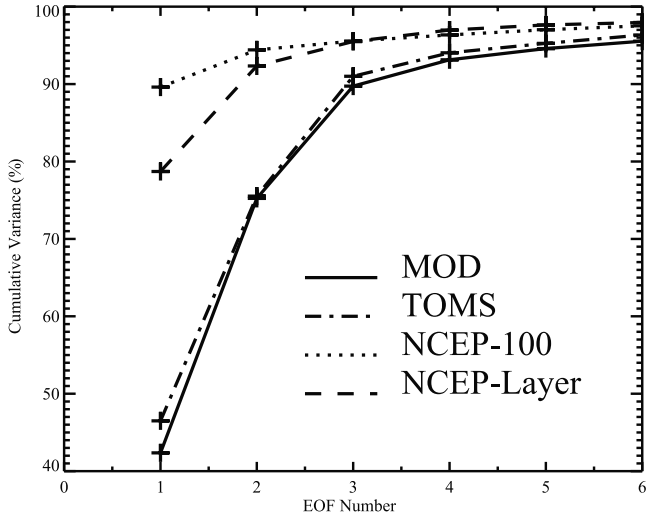

Figure 2. Cumulative variance as a function of number of EOFs.

[14] It is clear from Equation (3) that an arbitrary scaling factor can be applied to the EOFs, if it is simultaneously removed from each associated PC. One convention is to normalize the EOFs, $\|\mathbf{e}\| = 1$; then the variance of the associated PC will be equal to the associated eigenvalues. However, to present our results more clearly, we wanted the EOF patterns to have dimensional units. Therefore we have multiplied each EOF (and divided each PC) by the square root of their associated eigenvalue, i.e., the standard deviation of the conventional PC. Therefore our PCs have been normalized to have unity standard deviation, while the EOFs display typical values of the amplitude of oscillation at each grid point. The peak-to-trough amplitudes of the oscillations at any grid point can be recovered by taking the product of the EOF value and the peak-to-trough amplitude of the associated PC time series.

[15] Significance statistics for correlations between time series, such as PCs and indices, were generated by a Monte Carlo (bootstrap) method [*Press et al.*, 1992]. Three thousand isospectral surrogate time series (same power spectrum, randomized phases) were generated for each comparison to create a distribution of correlations. This distribution was transformed into an approximately normal distribution by the Fisher transformation [*Devore*, 1982]. The significance level of the actual (transformed) correlation within the transformed-correlation distribution was then determined.

4. Ozone EOFs

[16] EOF analyses were performed on the [25°S, 25°N] latitude band of the detrended, deseasonalized MOD and TOMS data sets. The patterns found in the decomposition of MOD are quite robust; analyses performed on other latitude bands have very similar patterns and symmetries. The TOMS analysis has the same features as the MOD analysis, although they appear in different combinations within the first few EOFs than they do in the MOD analysis. The relationship between the derived spatial patterns, their

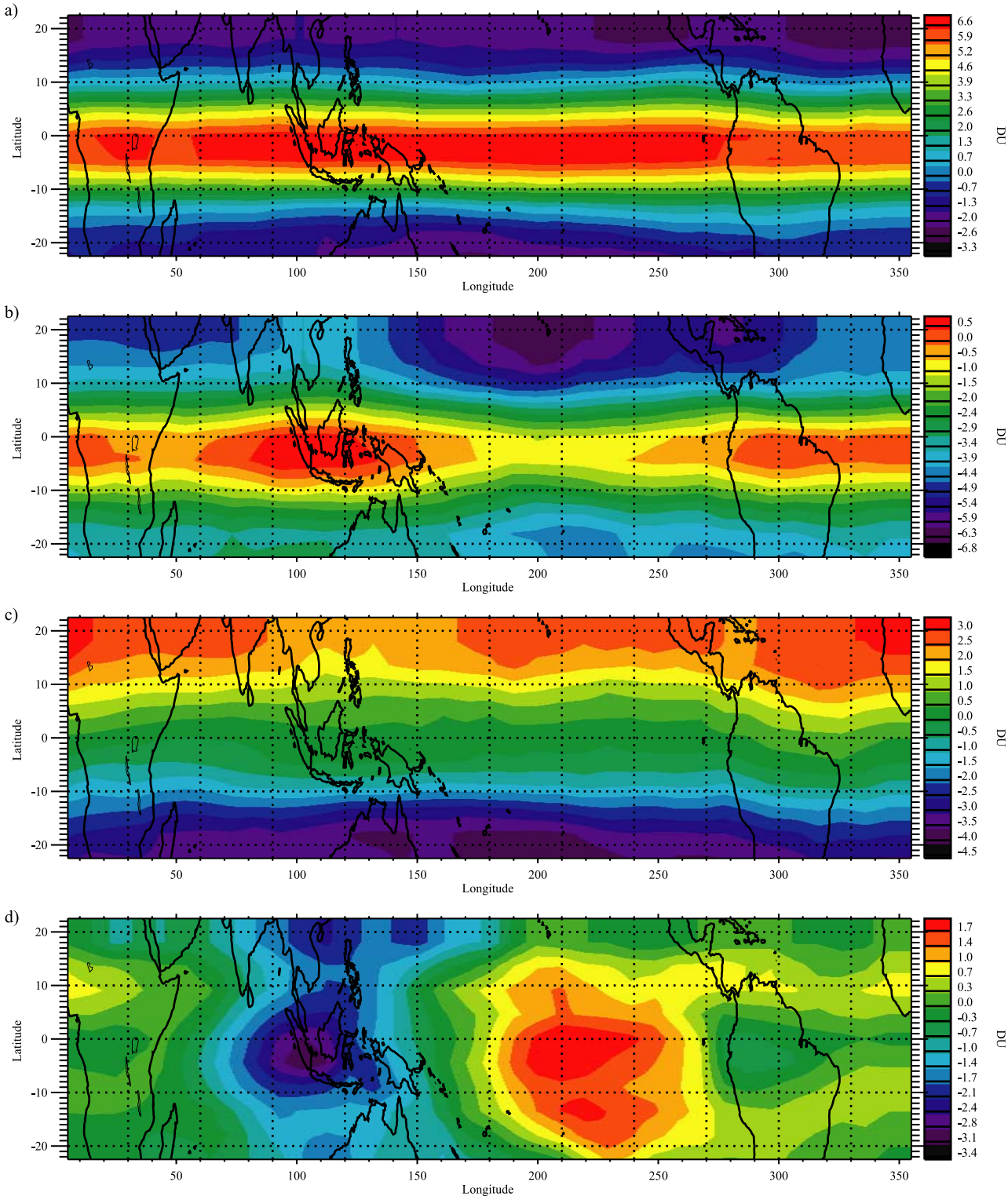

Figure 3. Spatial patterns for the first four MOD EOFs.

associated time series and physical processes will be discussed in Section 5.

4.1. Merged Ozone Data (MOD)

[17] The first four EOFs of the MOD data set together account for more than 93% of the variance, as shown by the solid line in Figure 2. The spatial patterns associated with these EOFs are shown in Figure 3. The associated PC time series and their Fourier spectra are shown in Figure 4. Each PC is shown in comparison to an appropriate index.

[18] The first EOF (MOD EOF1) captures 42% of the variance of MOD. It is basically a meridional arc show-

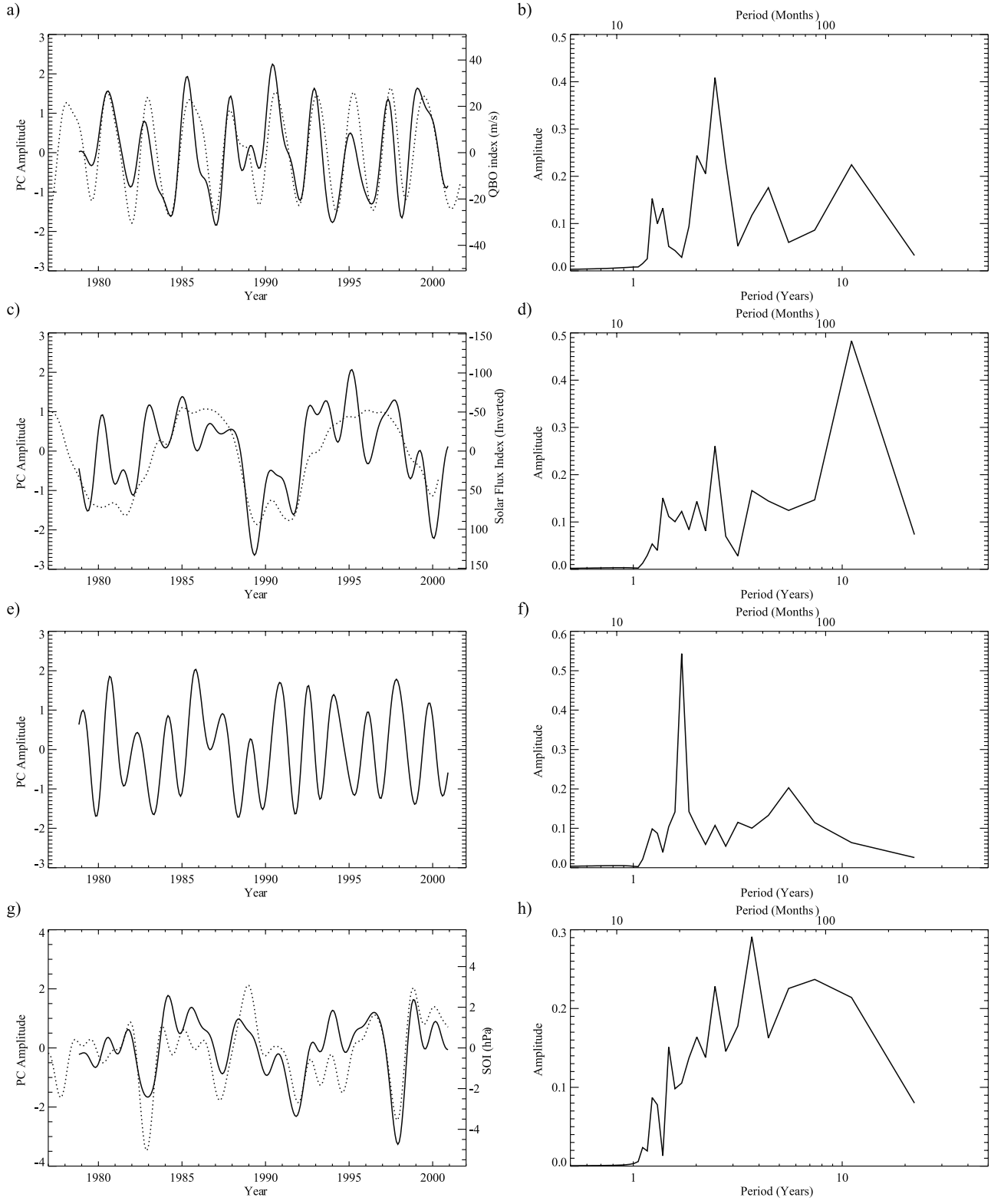

Figure 4. PC time series (left column) and spectra (right column) for the first four MOD EOFs. PCs (solid lines) are shown along with an appropriate index (dotted line). (a, b) PC1 and QBO index. (c, d) PC2 and inverted Solar Flux. (e, f) PC3. (g, h) PC4 and SOI.

ing zonal uniformity and symmetry about the equator. It oscillates about nodes at latitudes approximately 15° off the equator. The values shown range from a high of 7.0 Dobson units (DU) on the equator to a low of −2.8 DU at the northern boundary. The associated PC time series (MOD PC1), given in Figure 4a, shows the amplitude of the oscillation of this EOF in the MOD data set. A maximum peak-to-trough amplitude of approximately 28

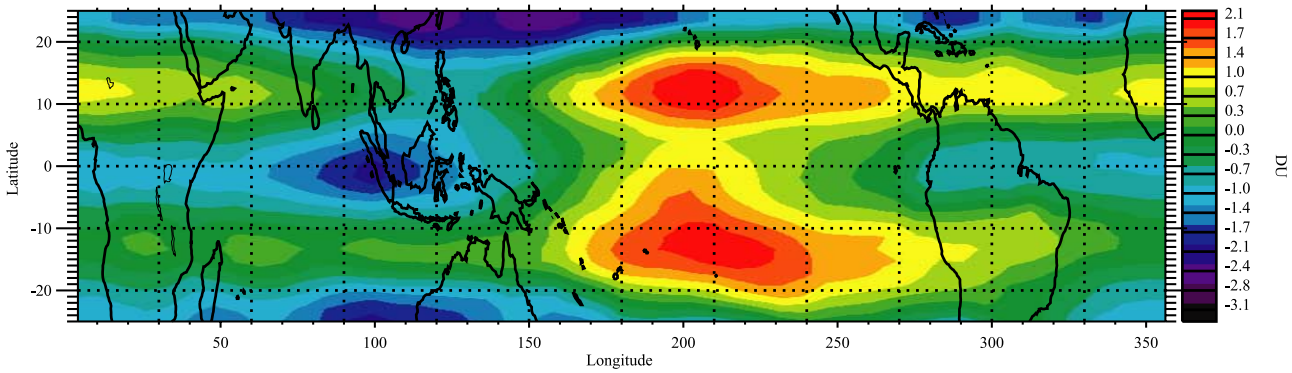

Figure 5. Spatial patterns for the fourth TOMS EOF.

DU occurs in the equatorial Pacific. The spectrum of the PC, Figure 4b, shows a dominant peak at 28 months with a secondary decadal signal. There are additional peaks at approximately 18 months and 4 years. Figure 4a shows the PC (solid line) compared to the QBO index (dotted line).

[19] A quick comment about the fine-scale features of the EOFs: While the maximum of MOD EOF1 actually appears to occur a couple of degrees south of the equator, we are reluctant to subscribe any significance to this asymmetry (as well as to other fine-scale behavior in this and following EOF patterns). Since MOD has 5° latitudes bins, we can only say that the maximum occurs between 2.5°N and 2.5°S. Furthermore, the fine-scale features are not robust between analyses, whereas the qualitative nature is robust.

[20] The second EOF (MOD EOF2) is similar to MOD EOF1 in that it is basically a zonally uniform and equatorially symmetric meridional arc, albeit with more zonal structure than MOD EOF1. It captures 33% of the variance of MOD. However, the pattern is almost entirely negative, barely breaking zero, and that only at the equator. The maximum of 0.9 DU lies on the equator and the minimum of −6.4 DU at the northern boundary. It is thus very similar to EOF1 except for a DC shift (i.e., a spatially constant offset). The associated PC (MOD PC2)is shown in Figure 4c. The spectrum of the PC, Figure 4d, has the same two primary peaks, 28 months and decadal, but the decadal is clearly dominant.

[21] The third EOF (MOD EOF3), capturing 15% of the variance, is a tilted plane oscillating about the equator. The pattern is still roughly zonally uniform, but it is now antisymmetric about the equator. Values range from 3.5 DU in the north to −4.1 DU in the south. The spectrum of the associated PC, shown in Figure 4f, has a single dominant peak at 21 months.

[22] The fourth EOF (MOD EOF4), capturing less than 4% of the variance, is the first occurrence of a pattern with strong zonal structure. Roughly symmetric about the equator, the EOF is a standing wave oscillating about nodes in the western and eastern Pacific. Values range from 2.1 DU in the central Pacific to −3.1 DU over Indonesia. The spectrum of the associated PC, Figure 4h, is fairly broad with its highest peak at a period of 4 years and substantial power in periods greater than 5 years.

[23] Analyses performed on MOD for the [20°S, 20°N] and [30°S, 30°N] latitude bands (not shown) display very similar results to the analysis of the [25°S, 25°N] band described above.

4.2. TOMS

[24] The EOF decomposition of the TOMS data set displays the same features as described above for the MOD analysis, albeit in a different combination. The TOMS data set has a finer spatial resolution than MOD, but a shorter time series. Therefore the EOFs show more detail, but the PCs are in general noisier and the spectra less resolved. In particular, with only 14 years of data, all correlations with decadal signals must be treated with great caution.

[25] The first four EOFs capture over 94% of the variance of TOMS with basically the same individual contributions as in the MOD decomposition; see Figure 2. The first three TOMS EOFs and PCs (not shown) contain the same basic structures as the equivalent MOD EOFs and PCs, but in a different combination than that seen in the MOD analysis. TOMS EOF1 shows a meridional arc and its associated spectrum shows the 28-month peak. TOMS EOF2 shows a combination of a tilted plane and a DC shift with its spectrum dominated by a broad low frequency band (7–10+ years) and a secondary peak at 20 months. TOMS EOF3 shows a tilted plane (its node slightly offset from the equator) and a dominant 20-month peak with a secondary low frequency signal. These are the same features that appear in the first three MOD EOFs and PCs but they have been shuffled somewhat. In the TOMS decomposition, the DC shift and decadal components are combined with the tilted plane and 20-month signals in the second and third EOFs/PCs, as opposed to with the meridional arc and 28-month signals as occurs in the first and second EOFs/PCs of the MOD analysis. This conflation of signals is discussed in detail in Section 5.2.

[26] Like MOD EOF4, the fourth TOMS EOF (Figure 5) is the first appearance of a pattern with a primarily longitudinal oscillation; however, it has a somewhat different structure. Both EOFs show rough equatorial symmetry and a zonal oscillation with nodes in the central and western Pacific. But in TOMS EOF4, there is a double-ridged symmetric structure with ridges at 12N, S and maxima at 150W that was not present at the lower spatial resolution of

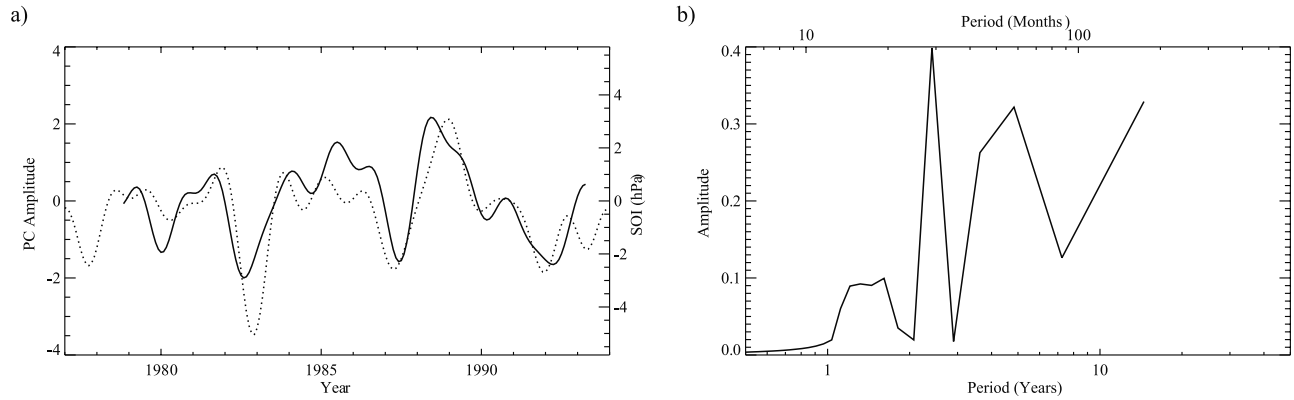

Figure 6. (a) PC time series and (b) spectrum for the fourth TOMS EOF. PC4 (solid) is compared to the SOI (dotted).

MOD EOF4. Furthermore, TOMS PC4, Figure 6a, has a much cleaner spectrum, Figure 6b, than its MOD counterpart, Figure 4h.

5. Analysis of the Ozone Decomposition

[27] The patterns seen in both the MOD and TOMS EOF decompositions can be closely tied to dynamical processes in the atmosphere. Most of the structure in the first four EOFs of both data sets can be attributed to three physical processes: the QBO, the interaction between the QBO and annual cycles, and ENSO. There is also substantial contribution from a process (or multiple processes) fluctuating on decadal time scales. With the exception of the decadal behavior and (to a much lesser degree) ENSO, the EOF analyses separate these processes into distinct EOFs. The correlations between indices for the physical processes and the PCs of both MOD and TOMS are listed in Table 2.

5.1. QBO and Decadal

[28] Ignoring for the moment the decadal signal, the dominant pattern seen in the first two EOFs of both data sets is the meridional arc structure oscillating with a period of 28 months. These are the spatial and temporal characteristics of the effect of the QBO on the ozone. Ozone is primarily created in the tropics of the middle stratosphere and carried poleward by the Brewer-Dobson circulation. This zonal mean meridional circulation is slow compared to the mean zonal wind. Therefore the spatial patterns of tracer transport associated with it should be zonally uniform to first order. During its westerly (easterly) phase, the QBO diminishes (enhances) the Brewer-Dobson circulation [*Plumb and Bell*, 1982; *Baldwin et al.*, 2001]. Therefore the tropical column ozone will increase (decrease) while the opposite will occur at higher latitudes. The phase change of this effect occurs at approximately 12° north and south of the equator [*Tung and Yang*, 1994a]. The pattern of both EOFs are roughly characteristic of the QBO, but the nodes of EOFs occur at the wrong latitudes. Furthermore, the appearance of two very similar EOFs and the conflation of the QBO and decadal signals obscures the connection to either process. These points will be revisited later in Section 5.2.

[29] The source of the decadal signal is an area of active research. One strong candidate is the decadal variation in the solar flux [*Chandra and McPeters*, 1994; *Shindell et al.*, 1999]. An increase in insolation leads to an increase in net ozone production. However, it has been demonstrated that this cannot account for all of the amplitude of the decadal variation [*WMO*, 1999]. Furthermore, the solar cycle appears to have a more complicated relationship with some of the other processes involved. For example, the length of the positive and negative phases of the QBO may be affected by the solar cycle [*Salby and Callaghan*, 2000].

[30] For better comparison to the QBO and Solar Flux indices, MOD PC1 and PC2 were filtered to isolate the two signals. The Bandpass A filter (Table 1) was used to remove the decadal contribution. The filtered PCs are compared to the QBO index in Figures 7a and 7c. The Lowpass C filter was used to remove the QBO contribution. Figures 7b and 7d show the results in comparison to the Solar Flux index. These indicate that MOD PC1 has a positive correlation with both the QBO and Solar Flux while MOD PC2 is

Table 2. Correlations Between TOMS and MOD PCs and Various Indices

PC #	Filter	Index	Corr.	Sig., %
		MOD PCs		
1	(none)	Solar Flux	0.26	84.3
	Lowpass C		0.80	91.4
	(none)	QBO	0.80	99.91
	Bandpass A		0.84	99.91
2	(none)	Solar Flux	−0.73	96.3
	Lowpass C		−0.87	94.2
	(none)	QBO	0.31	94.0
	Bandpass A		0.48	95.4
4	(none)	SOI	0.71	99.995
	Bandpass A		0.80	99.9998
		MOD-Band PCs		
1	(none)	QBO	0.84	99.8
		MOD-Low PCs		
1	(none)	Solar Flux	0.84	95.8
		TOMS PCs		
1	(none)	QBO	0.88	98.7
2	(none)	Solar Flux	0.80	99.6
	Lowpass C		0.95	99.91
3	(none)	Solar Flux	−0.25	93.6
	Lowpass C		−0.61	95.9
4	(none)	SOI	0.76	99.90

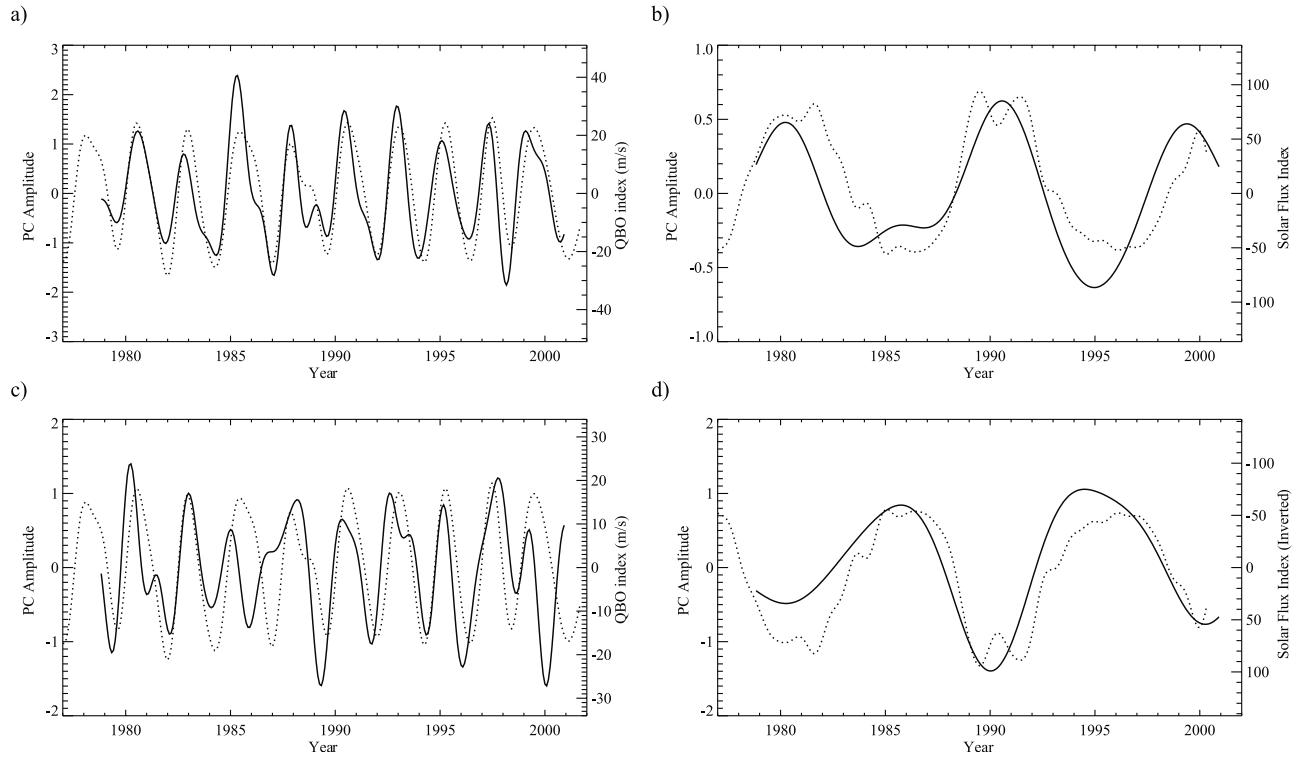

Figure 7. Comparisons of filtered PCs of the MOD EOFs (solid) to appropriate indices (dotted). (a) Bandpass A filtered PC1 and QBO index. (b) Lowpass C filtered PC1 and Solar Flux. (c) Bandpass A filtered PC2 and QBO index. (d) Lowpass C filtered PC2 and inverted Solar Flux.

correlated with the QBO but inversely correlated with the Solar Flux.

5.2. Separating the QBO and Decadal Signals

[31] The conflation of decadal and QBO signals in the first two EOFs and the appearance of similar patterns in the two orthogonal EOFs need further examination. It is unclear from the original EOF analysis whether the decadal signal is independent of the QBO time scale signal or if it is a low-frequency variation in the higher frequency signal. Since both EOFs are roughly zonally uniform, it is simpler to explore the zonal averages of the EOFs, shown in Figure 8a. MOD EOF2 (dashed line) is basically a constant shift of MOD EOF1. Recalling the filtered PCs, Figures 7a–7d, both MOD EOF1 and EOF2 are positively correlated with the QBO index. Therefore on QBO time scales, EOF1 and EOF2 oscillate in phase. But EOF2 is inversely correlated to the Solar Flux, while EOF1 is positively correlated, so on

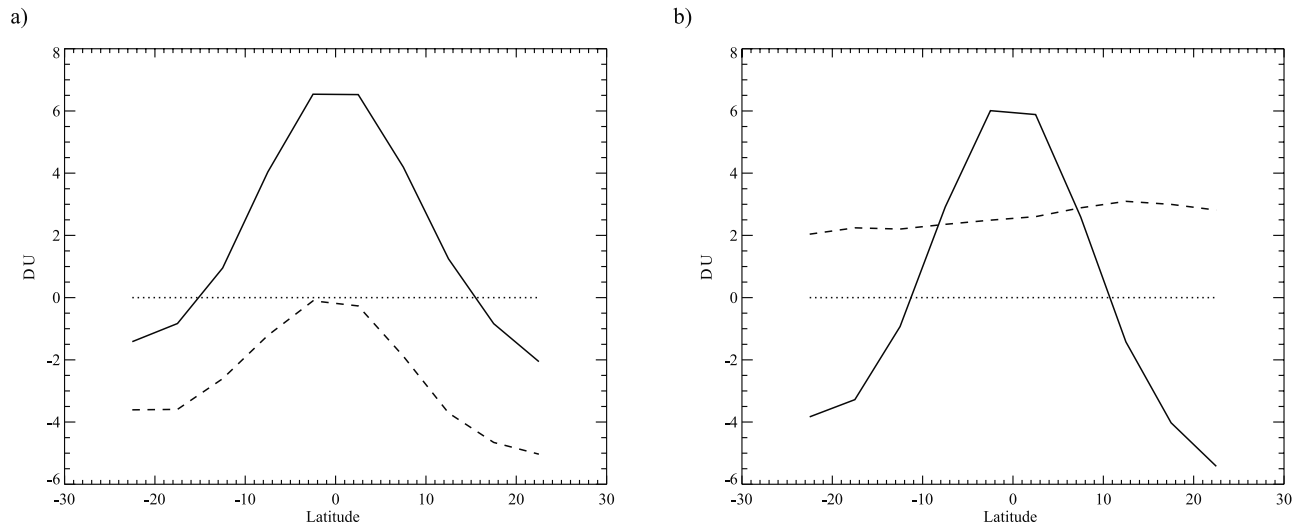

Figure 8. (a) Zonal averages of MOD EOF1 (solid line) and EOF2 (dashed line). (b) Weighted sum (solid line) and difference (dashed) of the MOD EOF1 and EOF2 zonal averages.

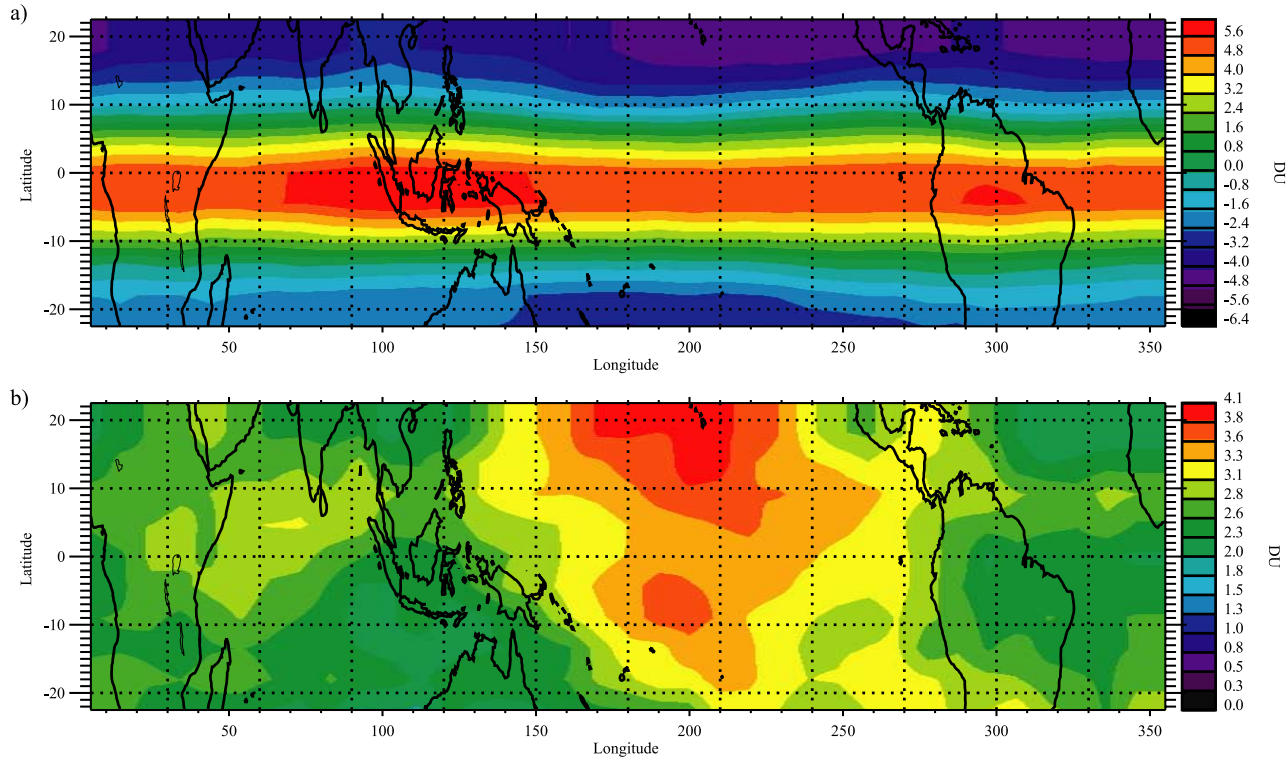

Figure 9. Leading EOFs from the filtered MOD analyses. (a) EOF1 of the Bandpass B filtered MOD (MOD-Band). (b) EOF1 of the Lowpass B filtered MOD (MOD-Low).

decadal time scales they oscillate a half period out of phase. Therefore the QBO contribution is the weighted sum of the two EOFs, while the decadal contribution is the weighted difference. The weights for the sum can be determined by finding the standard deviation of the Bandpass A filtered PCs. They roughly represent the portion of the amplitude of the oscillation of each EOF attributable to QBO time scales. The weights for the difference can be determined by finding the standard deviation of the Lowpass C filtered PCs and represent the portion attributable to decadal time scales. The weighted sum (solid line) and difference (dashed line) of the zonal averages calculated in the manner are shown in Figure 8b. This suggests that, for the combination of the first two EOFs, the QBO time scale signal is a meridional arc with nodes at approximately 11° off the equator, while the decadal signal is roughly a flat plane with no nodes. The same procedure can be performed with the full EOFs instead of the zonal averages and an associated time series can be found by projecting the original data onto these constructed patterns. However, these patterns and time series will no longer be mutually orthogonal.

[32] A more rigorous way to separate the decadal and QBO time scale signals is to filter the data for the desired frequencies *prior* to performing the EOF analysis. It should however be noted that disadvantages of this method include the loss of the ability to examine long-term fluctuations of shorter time scale features and the possible distortion of highly non-sinusoidal signals when narrow-bandwidth Fourier filtering is applied. These caveats notwithstanding, this procedure is a useful confirmation of the previous linear combination method. This procedure was performed using the Bandpass B and Lowpass B filters described in Table 1. The leading EOFs of the resulting analyses are shown in Figure 3. These EOFs are very similar to those found by the linear recombinations of the full (2D) MOD EOF1 and EOF2 (data not shown).

[33] The first two EOFs of the Bandpass B filtered MOD (MOD-Band), capturing 81% of the variance of the filtered data set, display patterns associated with the QBO without the interference from any decadal process(es). Obvious signs of ENSO are also removed, although higher harmonics of ENSO's fundamental period may still be present. These harmonics are discussed later in more depth.

[34] The first EOF, Figure 9a, captures 61% of the variance. It shows the QBO pattern with nodes at approximately 12° off the equator. Values range from 6.3 DU at the equator to −4.8 DU at the northern boundary. The associated PC (data not shown) correlates well with the QBO index; see Table 2. Its spectrum is very similar to the portion of the MOD PC1 spectrum contained between periods of 1 to 3 years; see Figure 4b. The second EOF (data not shown) captures 20% of the variance. It shows a tilted plane pattern similar to that of MOD EOF3, Figure 3c. This pattern is characteristic of the QBO-annual beat, described later in this section. Values are similar, ranging from 3.6 DU in the north to −2.8 DU in the south, and there a little more longitudinal structure. The spectrum of the associated PC shows a clean peak at 21 months, again similar to MOD PC3, Figure 4f.

[35] The first EOF of the Lowpass B filtered MOD (MOD-Low), Figure 9b, captures over 76% of the variance of the filtered data. It is roughly a flat plane with no nodes; values are strictly positive, ranging from 4.0 DU to 2.0 DU.

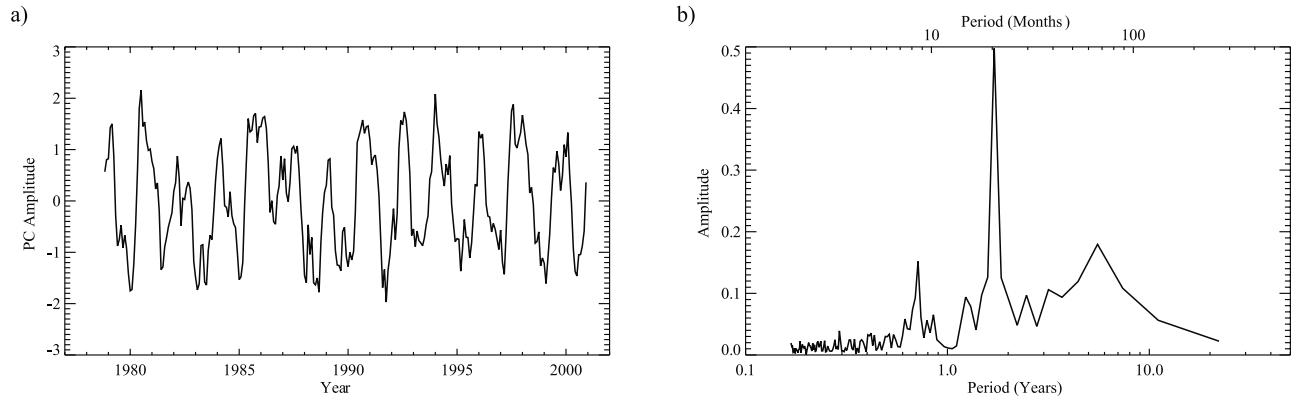

Figure 10. (a) PC time series and (b) spectrum for the third EOF from the Bandstop A filtered MOD data (MOD-Notch).

This DC component seems to be a consistent feature of the patterns associated with decadal variability. The associated PC correlates well with the Solar Flux index; see Table 2. Its spectrum shows a strong decadal peak and a weaker broad peak at 3.5–4.5 year periods. This is probably due to ENSO and is the likely source of much of the longitudinal variability of this EOF. The decadal signal could be separated from the ENSO signal by a tighter filter, e.g., the Lowpass C filter. However, this restrictive a filter would leave very few degrees of freedom in the resulting time series, so the resulting EOF analysis may not be very robust.

5.3. QBO-Annual Beat

[36] The third MOD EOF displays a tilted plane oscillating about a node at the equator with a period of 21 months. These are spatial and temporal characteristics of the interaction between the QBO and annual cycles. The modulation of the annual meridional transport by the tropical QBO results in the creation of two beat oscillations with frequencies equal to the sum and difference of the QBO and annual frequencies; i.e., at periods of 21 and 8.4 months [*Tung and Yang*, 1994a; *Baldwin et al.*, 2001]. While this process is primarily an extra-tropical one, its effects can be seen inside the (25°S, 25°N) band of this study. However, the interaction between the QBO and any annual cycle (e.g., the annual cycle in ozone production) has the potential to create identical beat frequencies. Modeling work to determine the correct phase of the beat oscillations as well as their amplitudes may help determine which annual cycle is responsible for the beat frequency seen here.

[37] Since the data for these analyses have been lowpass filtered for periods above 15 months, only the 21-month beat appears in these EOFs. To determine if the high-frequency beat can be resolved, we redid the EOF analysis of the MOD data using Bandstop Filter A (MOD-Notch) instead of Lowpass Filter A. In this analysis, only periods between 15 and 9.5 months are damped or removed. The bandstop filter was used to remove the shoulders of the annual cycle peak that remained after the mean annual cycle was removed. The resulting EOFs were nearly identical to those found in the analysis of the lowpass filtered MOD except that the percentage of the variability explained by the first four EOFs dropped by about 10%. This is not due to a decrease in the absolute variance explained, but rather to the approximately 10% increase in total variance of the data set caused by the presence of the high-frequency signals. The PC of the third EOF, shown along with its spectrum in Figure 10, contains the signal of both the 21-month and 8.4-month beat interactions.

[38] In the TOMS analysis, both PC2 and PC3 display the characteristic 20-month frequency of the QBO-annual beat, but they also have a decadal component. The spatial structures are tilted planes offset from each other by a DC shift. This is analogous to the conflation of QBO and decadal seen in the MOD analysis and they can be separated in a similar manner.

5.4. ENSO

[39] The fourth EOFs of the MOD and TOMS sets display a zonal wavenumber-1 oscillation with extrema in the central Pacific and near Indonesia. The spectra show peaks at periods around 4–5 years, but there is a broad range of frequencies with substantial power. This is strongly suggestive of the spatial and temporal characteristics of the (highly non-sinusoidal) ENSO process. Comparisons to the SOI index confirm that these EOFs are dominated by ENSO. The noisiness of the EOF and PC in the MOD data set can be at least partially attributed to the low spatial resolution. A much cleaner ENSO signal is seen in the TOMS data set EOFs. The TOMS EOF4 has the characteristic bimodal structure in the central Pacific and the spectrum of TOMS PC4, Figure 6b, clearly shows the set of harmonic frequencies of the fundamental 56-month frequency [*Jiang et al.*, 1995; *Ghil and Robertson*, 2000]. The presence of the bimodal structure in the TOMS EOF4 means that only processes with such structure, such as ENSO, will strongly project onto this EOF. Therefore the resulting PC has a cleaner signal and spectrum. For the ENSO signal, the increased spatial resolution of the TOMS data has thus overcome the limitations inherent in its shorter time series.

[40] One possible source of the ENSO signal in ozone is the induced variation in tropospheric ozone due to changes in western Pacific convection patterns and to biomass burning. Another possible source is the induced variation in the tropopause height. During El Niño years, i.e., negative SOI, increased convection in the central Pacific raises the tropopause height. This, in turn, causes a decrease

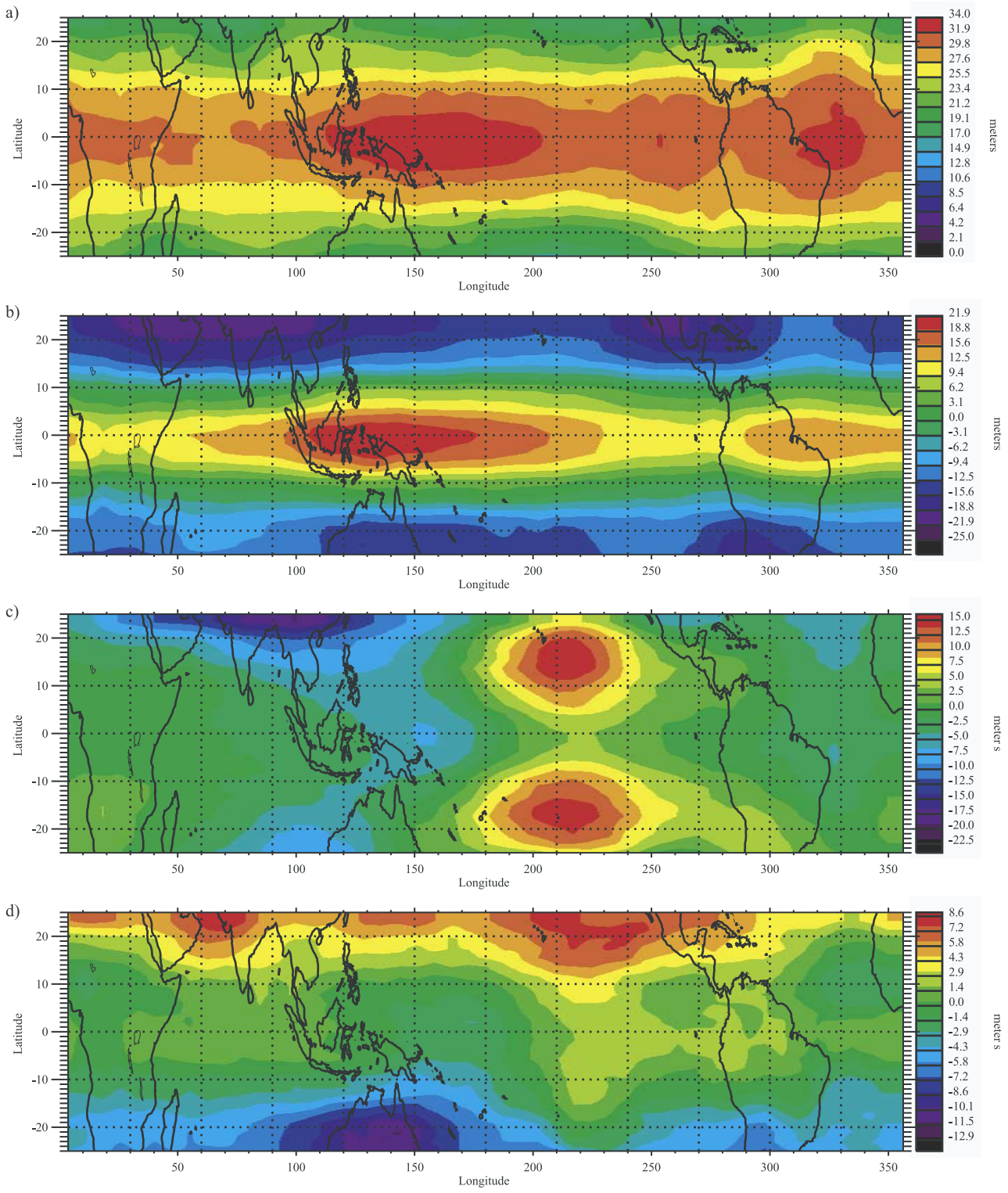

Figure 11. Spatial patterns for the first four EOFs from the NCEP-NCAR reanalysis 30 hPa to 100 hPa layer thickness (NCEP-Layer).

in total column ozone. A vertical perturbation in the tropopause in the tropics generally coincides with a vertical perturbation in an isentropic surface. The relatively rapid movement of air along an isentropic surface mixes air at the higher elevation of the perturbation with the surrounding lower air. Since the ozone concentration generally increases with height near the tropopause, this mixing lowers the ozone concentration at the perturbation while raising the concentration in the surrounding air. This is a similar mechanism to that proposed in *Salby and Callaghan*

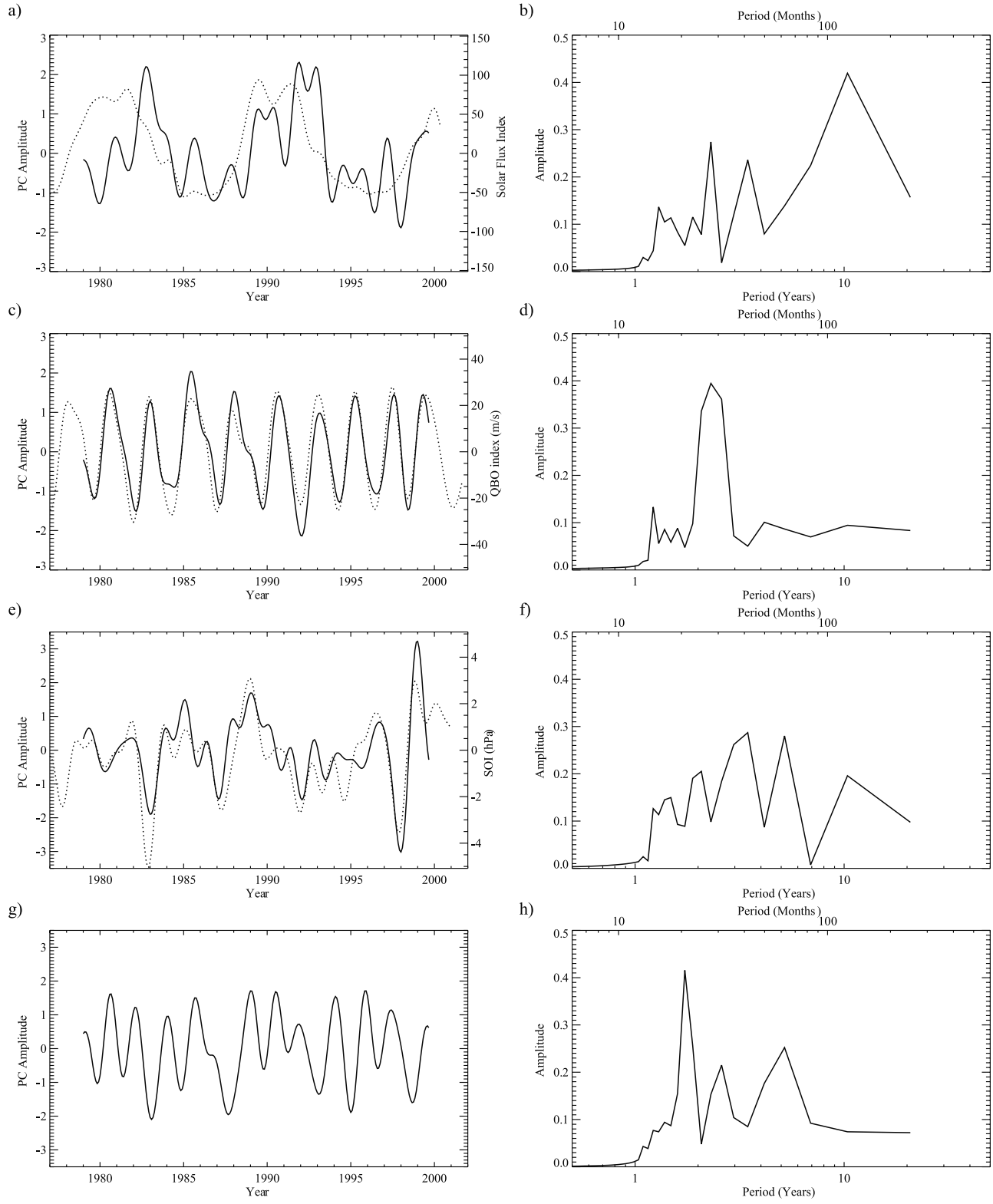

Figure 12. PC time series (left column) and spectra (right column) for the first four NCEP-Layer EOFs. PCs (solid lines) are shown along with the appropriate index (dotted line). (a, b) PC1 and Solar Flux. (c, d) PC2 and QBO. (e, f) PC3 and SOI. (g, h) PC4.

[1993] for ozone variations on synoptic time scales. During La Niña years, i.e., positive SOI, the opposite will occur, causing a relative increase in total column ozone over the central Pacific.

[41] ENSO probably has a projection onto the first MOD EOF as well. It is the likely source of the 4–5 year period fluctuation seen in the MOD PC1, Figures 4a–4b. Furthermore, the double peak at ~16 months is consistent with ENSO's ~16-month 2nd harmonic. The signal of the first harmonic of ENSO, at ~2–2.5 years, would be obscured by the dominant QBO peak. Since the structure of this oscillation is zonally uniform, it would correspond to the overall warming of the tropics that occurs during El Niño years. This effect on the ozone column is most likely due to tropopause height variations rather than biomass burning, since the latter has a large longitudinal variation.

6. Analysis of NCEP-NCAR Data

[42] For comparison to structures in dynamical variables, similar analyses were performed on various fields from the NCEP-NCAR reanalysis product. To examine the behavior near the tropopause, we performed an EOF decomposition on the geopotential height of the 100 hPa pressure surface (NCEP-100). To examine the behavior in the stratosphere, we performed an EOF analysis on the thickness of the layer determined by differencing the geopotential heights of the 30 hPa and 100 hPa pressure surfaces (NCEP-Layer). The 30 hPa level is near the region of maximum ozone density within the column. Ozone is the principal absorber of solar UV radiation in the stratosphere [*Goody and Yung*, 1989]. An increase in ozone concentration would result in an increase in the stratospheric heating rate, and hence the temperature. Near 100 hPa, the temperature is dynamically controlled and is expected to be insensitive to ozone heating. However, near 30 hPa the temperature is radiatively controlled. Therefore increases (decreases) in the ozone of the lower stratosphere will induce thermal expansion (contraction) of the lower stratosphere. The results, particularly for the NCEP-Layer analysis, are probably caused by a combination of the direct effect of the physical processes on the dynamical variables and an indirect effect using chemical species such as ozone as an intermediary.

6.1. Layer Thickness EOFs

[43] The first four EOFs of the NCEP-Layer data capture over 97% of the variance. They show roughly the same basic structures seen in the ozone analyses, except that patterns of the third and fourth NCEP-Layer EOFs correspond to the fourth and third ozone EOFs, respectively. Furthermore, with its finer spatial resolution, NCEP EOF3 displays a bimodal structure closer to that of TOMS EOF4, rather than to the equatorially-centered structure of MOD EOF4. The spatial patterns are shown in Figure 11, associated PC time series and spectra in Figure 12 and correlations in Table 3.

[44] As in the ozone analyses, the first two EOFs (capturing 79% and 14% of the variance, respectively) show the meridional arc structure associated with the QBO. However, there is a strong spatial DC shift in the first EOF, Figure 11a. It is strictly positive with values ranging from 34 meters on the equator in the central Pacific to 17 meters on the north and south boundaries. There is also substantially more zonal variation than was seen in the first EOFs of the ozone data. The second EOF, Figure 11b, is the more standard shape with nodes occurring at an average of ~11° off the equator. The spectrum of the first PC, Figure 12b, shows peaks at decadal and QBO periods but is in general noisier than the comparable spectrum from MOD PC1. Figure 13 shows the results of Bandpass A and Lowpass C filtering on NCEP-Layer PC1 and PC2. As in the ozone EOFs, NCEP-Layer PC1 and PC2 are positively correlated with each other on QBO time scales and inversely correlated on decadal time scales. Zonal averages and their weighted sum and difference are shown in Figure 14. The QBO time scale behavior is a meridional arc, with a maximum of the equator of 37 m, while the decadal time scale behavior is relatively flat. However, unlike the ozone results, the QBO structure does not recover the ~12° nodes seen in the ozone analysis; it is almost entirely positive with a node at ~22°S and not quite reaching zero by the northern boundary at 25°N. It is not clear if this spatial DC shift on QBO time scales is a real physical behavior, an artifact of the NCEP-NCAR reanalysis data or an artifact of the EOF analysis. It is possible that later EOFs could compensate for this shift, although the decreasing amplitude of subsequent EOF eigenvalues make this somewhat unlikely.

[45] The ENSO and QBO-annual beat patterns appear in the NCEP-Layer analysis in opposite order to that of the ozone analyses. The third NCEP-Layer EOF, Figure 11c, captures 3% of the variance and shows the zonal oscillation associated with ENSO while the fourth, Figure 11d, captures 1.5% of the variance and shows the tilted plane of the QBO-annual beat. Compared to MOD EOF3, there is substantially more zonal variation in NCEP-Layer EOF4. This can be primarily ascribed to the small percentage of variability that it captures; it is much closer to the background noise level.

[46] We can investigate the relative importance of ozone fluctuations in the NCEP-Layer results by making a rough calculation of the expected amplitude of the thermal expansion caused by solar absorption. An approximate estimate

Table 3. Correlations Between NCEP-NCAR Reanalysis PCs and Various Indices

PC #	Filter	Index	Corr.	Sig., %
		NCEP-Layer PCs		
1	(none)	Solar Flux	0.43	84.6
	Lowpass C		0.60	84.5
	(none)	QBO	0.20	86.8
	Bandpass A		0.30	88.4
2	(none)	Solar Flux	−0.15	92.3
	Lowpass C		−0.50	84.1
	(none)	QBO	0.92	99.997
	Bandpass A		0.94	99.9993
3	(none)	SOI	0.82	99.9999
		NCEP-100 PCs		
1	(none)	Solar Flux	0.22	83.5
	Lowpass C		0.66	91.6
	(none)	SOI	−0.43	96.7
	Bandpass A		−0.54	99.2
2	(none)	Solar Flux	−0.29	77.9
	Lowpass C		−0.40	75.2
	(none)	SOI	−0.72	99.997
	Bandpass A		−0.70	99.99

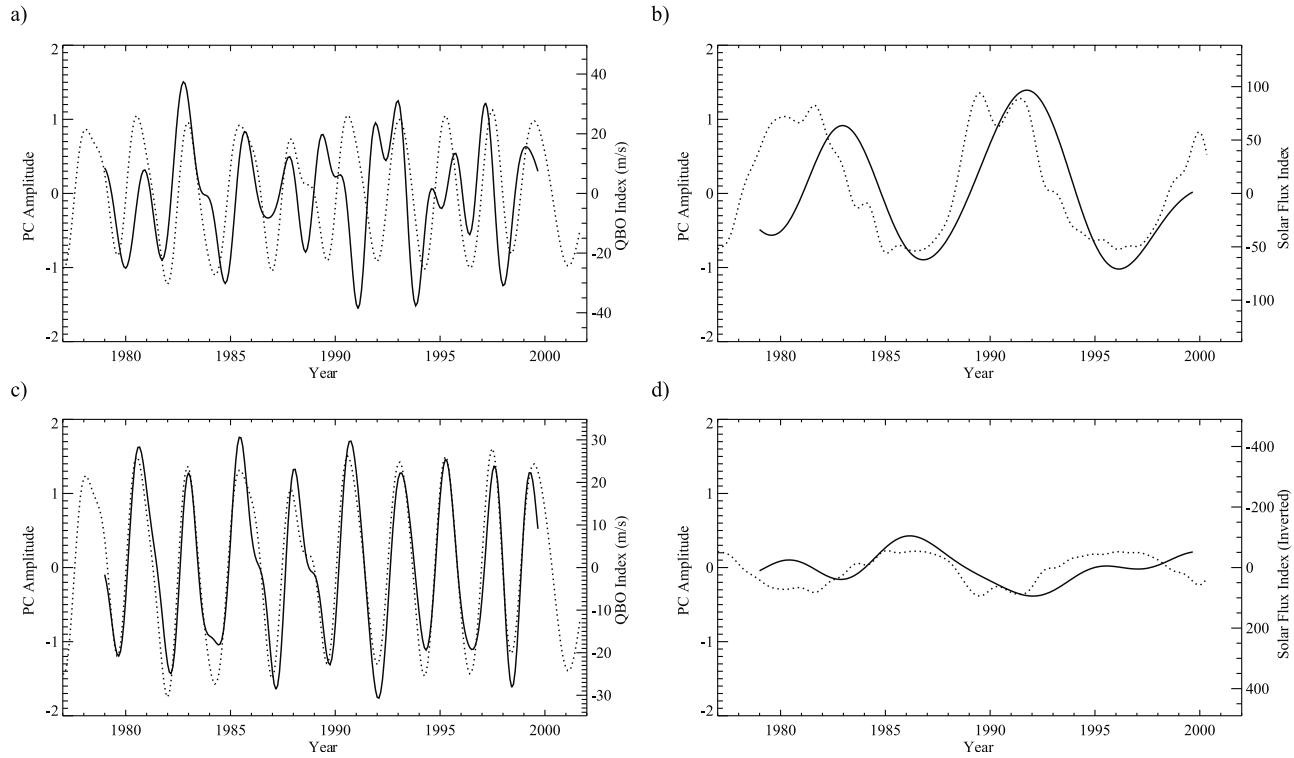

Figure 13. Comparisons of filtered PCs of the NCEP-Layer EOFs to appropriate indices. (a) Bandpass A filtered PC1 and QBO index. (b) Lowpass C filtered PC1 and Solar Flux. (c) Bandpass A filtered PC2 and QBO index. (d) Lowpass C filtered PC2 and inverted Solar Flux.

based on radiative equilibrium yields 1°K increase for every 10 DU increase in ozone column; see Figures 14 and 15 of *McElroy et al.* [1974]. A change in the NCEP-NCAR reanalysis geopotential height of about 10 m corresponds to a 0.3°K change. The latter change can be caused by an increase of 3 DU in ozone column. We see a 37 m change in the NCEP-Layer results, see Figure 14b, corresponding to a 7 DU change in the MOD results, Figure 8b. Therefore ozone heating is a important source of the variability seen in the NCEP-Layer data, but other processes such as dynamically forced heating are likely to play a comparable role.

6.2. 100 hPa Surface EOFS

[47] To examine behavior near the tropopause, an EOF decomposition was performed on the NCEP-NCAR reanalysis 100 hPa geopotential height field (NCEP-100). Spatial patterns from the first two EOFs are shown in Figure 15, associated PC time series in Figure 16 and correlations in

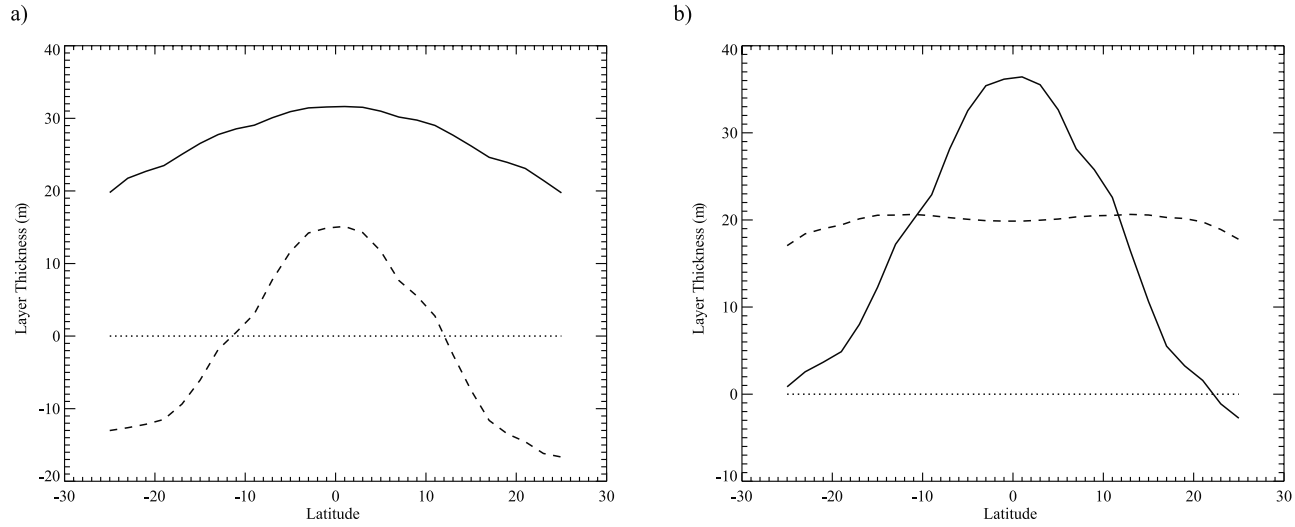

Figure 14. (a) Zonal averages of NCEP-Layer EOF1 (solid line) and EOF2 (dashed line). (b) Weighted sum (solid line) and difference (dashed) of the NCEP-Layer EOF1 and EOF2 zonal averages.

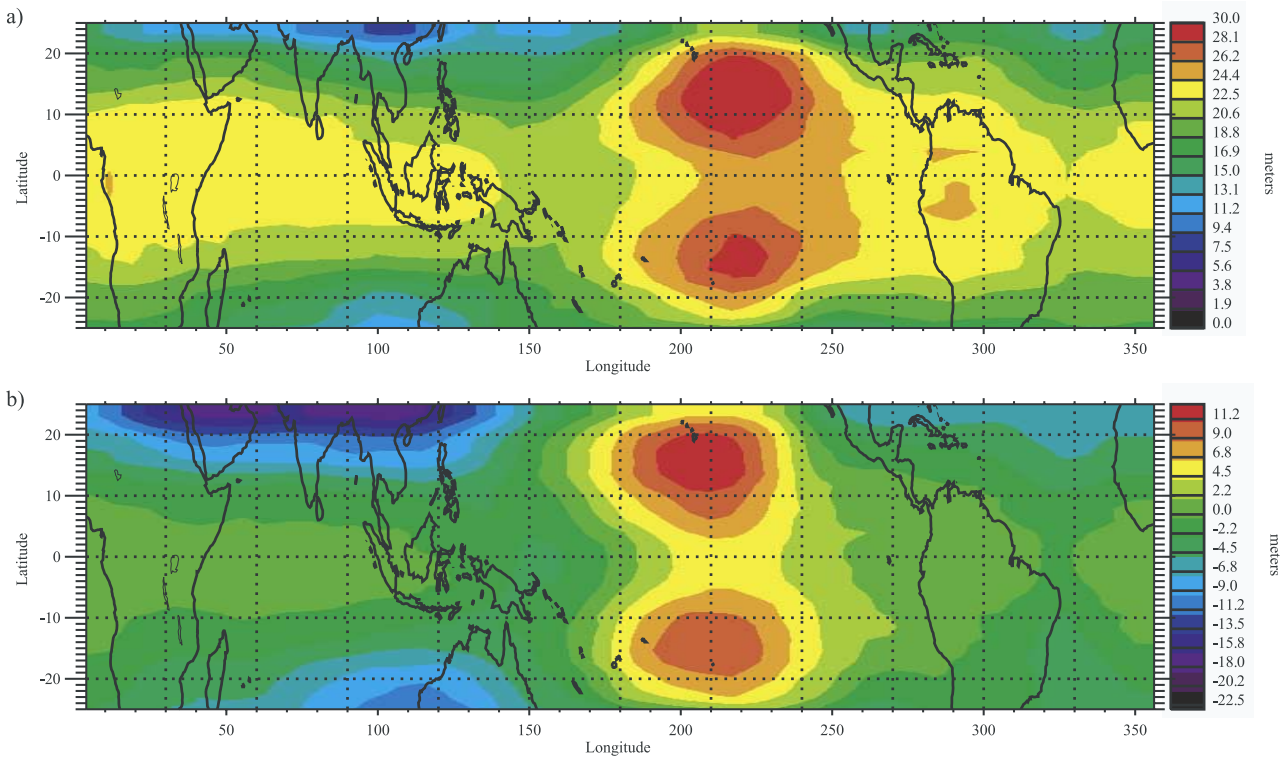

Figure 15. Spatial patterns for the first two EOFs from the NCEP-NCAR reanalysis 100 hPa geopotential height data (NCEP-100).

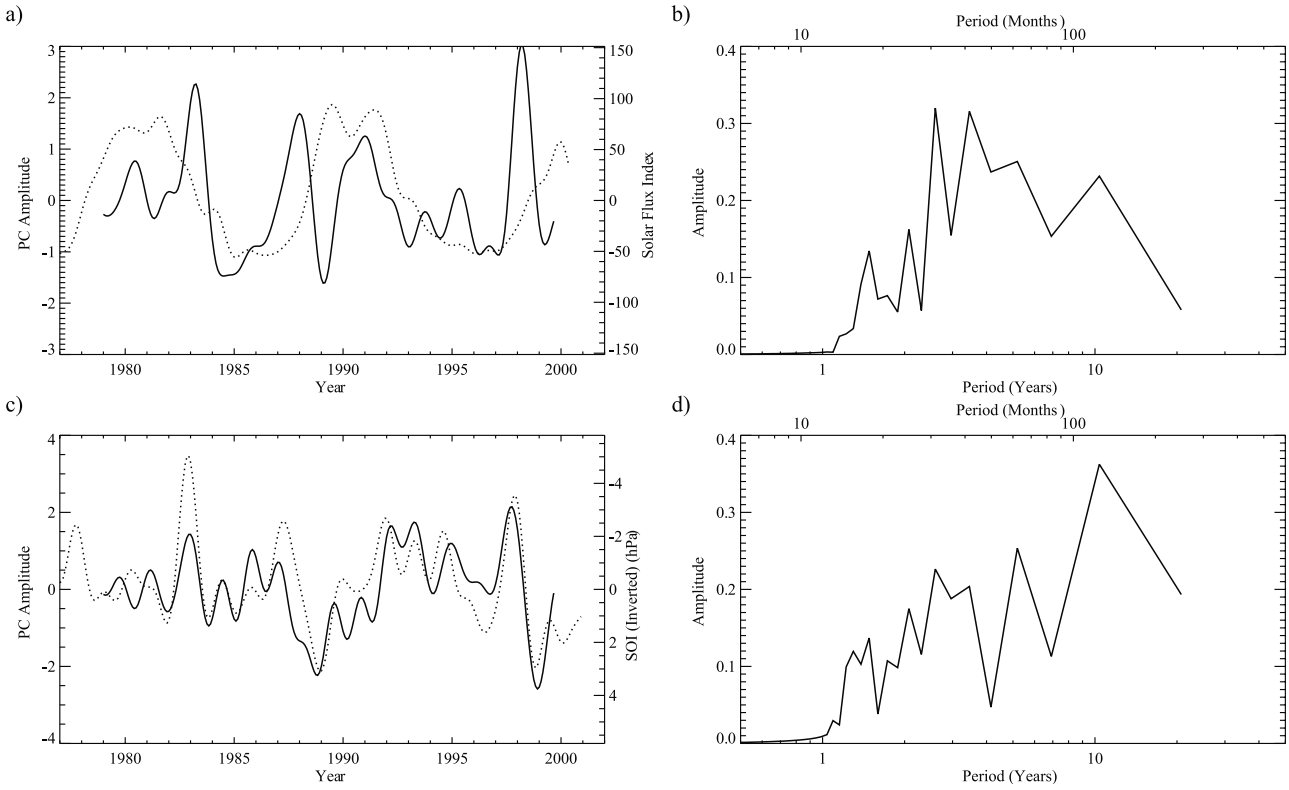

Figure 16. PC time series (left column) and spectra (right column) for the first two NCEP-100 EOFs. PCs (solid lines) are shown along with the appropriate index (dotted line). (a, b) PC1 and Solar Flux. (c, d) PC2 and inverted SOI.

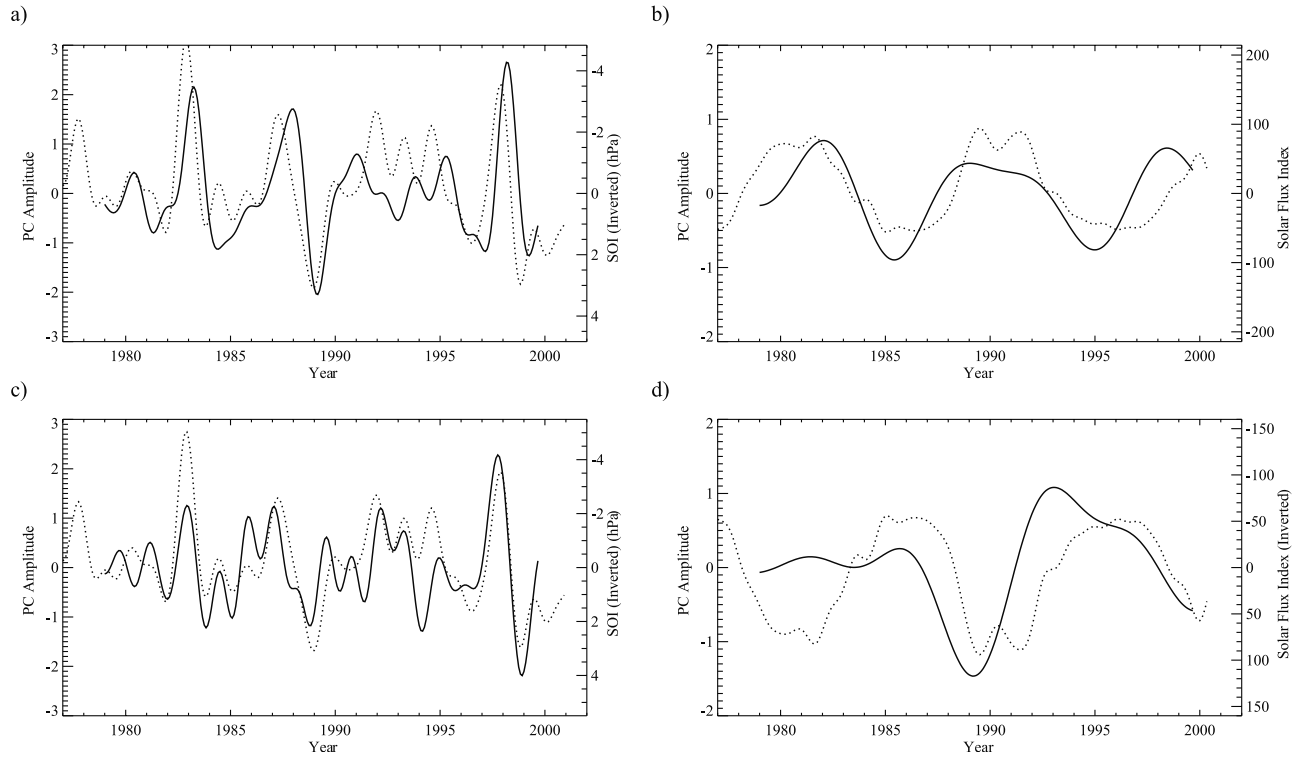

Figure 17. Comparisons of filtered PCs of the NCEP-100 EOFs to appropriate indices. (a) Bandpass A filtered PC1 and inverted SOI. (b) Lowpass C filtered PC1 and Solar Flux. (c) Bandpass A filtered PC2 and inverted SOI. (d) Lowpass C filtered PC2 and inverted Solar Flux.

Table 3. The first EOF, by itself, captures over 89% of the variance. The spatial pattern, Figure 15a, consists of a large zonal oscillation and a meridional arc superimposed upon a relatively flat plane. Note that the values of the EOF are all positive, ranging from a maximum of 31 meters to a minimum of 8 meters. The second EOF, capturing less than 5% of the variance, has a similar pattern without the spatial DC shift. Both PCs show evidence of ENSO and decadal oscillations.

[48] Bandpass filter A and Lowpass filter C were applied to the PCs to separate these effects. The resulting time series, along with appropriate indices, are shown in Figure 17. They show that NCEP-100 PC1 and PC2 oscillate with opposite phases on decadal time scales but in phase on shorter time scales. This is analogous to the conflation of decadal and QBO signals seen in the MOD analyses. The second EOF enhances the internal structure of the first EOF on the faster time scale, while suppressing it on the decadal time scale. Therefore the decadal behavior (correlated with Solar Flux) contains less of the zonal and meridional variability; it is dominated by the DC component. The zonal and meridional variability occur primarily on the shorter time scales (inversely correlated with SOI). However, as in the NCEP-Layer analysis, a substantial spatial DC shift at shorter time scales still remains.

[49] Comparing the ENSO-related patterns of these results to those found in the MOD analysis, we can see that NCEP-100 PC1 and PC2 have an inverse correlation with the SOI, while MOD PC4 has a positive correlation (Figure 7g). Therefore for the variations associated with ENSO, the 100 hPa geopotential height and the column ozone anomaly are inversely correlated. This is consistent with the explanation given in Section 5.4. A rough estimate of the expected change in the ozone column caused by these fluctuations in tropopause height can be made. *Stephenson and Royer* [1995] reported about 1 DU increase for every 5 m decrease in the 200 hPa geopotential height. Scaling from their result, we estimate that a 10 m change in geopotential height could cause about 2 DU change in column ozone. This is consistent with our MOD and NCEP-100 results if we compare the relative fluctuations within the NCEP-NCAR reanalysis EOFs, but cannot account for the lack of response to the DC component of NCEP-100 EOF1.

[50] Comparing the patterns associated with decadal variation from the MOD and NCEP-100 analyses, we find a different behavior. Both datasets display a positive correlation with solar flux; therefore the 100 hPa geopotential height and the column ozone anomaly are positively correlated for the tropical latitudes studied. This is consistent with the model results from *Shindell et al.* [1999] and *Hood* [1997]. A possible component of this difference in behavior may be the difference in the patterns associated with decadal and ENSO oscillations. The ENSO pattern has relatively steep gradients, while decadal pattern is primarily a flat DC oscillation. so little tilting of isentropic surfaces is expected on decadal time scales; so the mechanism described for the ENSO-related variability would not be invoked.

7. Conclusions

[51] We have shown the spatial-temporal patterns of tropical column ozone variability on interannual time scales.

To our knowledge, this is the first time longitudinal, latitudinal and temporal behavior has been simultaneously examined. Spatial patterns relating to the fluctuations of the QBO, QBO-annual beat and ENSO have been identified and decadal oscillations examined. The structure of these patterns appears in the ozone record quite robustly (with a reshuffling of the components in the TOMS analysis) and in the NCEP-NCAR reanalysis fields as well, albeit with less fidelity.

[52] We have been able to distinguish the meridional shape of the QBO, i.e., the meridional arc, from the relatively flat plane oscillating on decadal time scales. The decadal fluctuations in ozone oscillate in phase with the 11-year solar cycle but the shortness of the ozone record precludes the confirmation of the connection.

[53] Three oscillations associated with the QBO have been identified: the standard 28-month cycle and the 20-month and 8.6-month QBO-annual beats. The equatorially asymmetric spatial pattern of the QBO-annual beat has been isolated from the symmetric one of the 28-month cycle. Both patterns show the expected zonal uniformity, and the meridional phase transition of the QBO signal at $\sim 12°$ off the equator has been recovered as well. A time series relating to the QBO-annual beat has been determined thereby allowing questions of the phase of this oscillation to be addressed in later work.

[54] The effect of ENSO on the ozone column has also been identified. It is a testament to the precision of the TOMS and MOD data sets that such a small signal, $\sim 1\%$ of total column ozone, is seen so clearly. A mechanism linking the column ozone abundance to the ENSO cycle through the variation of tropopause height has been proposed, but separation of this process from the effects of tropospheric ozone variations induced by ENSO is beyond the scope of this study.

[55] This work constitutes a preliminary study of each of these processes, particularly for the decadal signal. We have primarily focused on matching the phase and periods of the signals, while discussing the qualitative nature of the spatial patterns. Future work should include quantitative studies of the amplitudes of the oscillations and comparisons to modeling studies. The extension of this analysis to higher latitudes is also desirable.

[56] **Acknowledgments.** We thank M. Allen, D. Noone, S. Leroy, P. Wennberg, A. Ingersoll, T. Schneider, A. Gould, Z. Kuang, X. Huang and three anonymous reviewers for helpful comments, and R. Stolarski of NASA Goddard Space Flight Center for the use of O_3 data from the merged ozone data set. Supported by NASA grants NAG5-10901 and NAG1-2081 to the California Institute of Technology.

References

Baldwin, M. P., et al., The quasi-biennial oscillation, *Rev. Geophys.*, *39*, 179–229, 2001.

Brasseur, G. P., J. J. Orlando, and G. S. Tindall (Eds.), *Atmospheric Chemistry and Global Change*, 654 pp., Oxford Univ. Press, New York, 1999.

Chandra, S., and R. D. McPeters, The Solar-Cycle Variation of Ozone in the Stratosphere Inferred from Nimbus-7 and NOAA-11 Satellites, *J. Geophys. Res.*, *99*, 20,665–20,671, 1994.

Devore, J. L., *Probability and Statistics for Engineering and the Sciences*, 1st ed., 640 pp., Brooks/Cole, Monterey, Calif., 1982.

Ghil, M., and A. W. Robertson, Solving problems with GCMs: General circulation models and their role in the climate modeling hierarchy, in *General Circulation Model Development: Past, Present and Future*, edited by D. Randall, pp. 285–325., Academic Press, San Diego, Calif., 2000.

Goody, R. M., and Y. L. Yung, *Atmospheric Radiation: Theoretical Basis*, 2nd ed., 519 pp., Oxford Univ. Press, New York, 1989.

Herman, J. R., R. McPeters, R. Stolarski, D. Larko, and R. Hudson, Global average ozone change from November 1978 to May 1990, *J. Geophys. Res.*, *96*, 17,297–17,305, 1991.

Hood, L. L., The solar cycle variation of total ozone: Dynamical forcing in the lower stratosphere, *J. Geophys. Res.*, *102*, 1355–1370, 1997.

Jiang, N., J. D. Neelin, and M. Ghil, Quasi-quadrennial and quasi-biennial variability in the equatorial Pacific, *Clim. Dyn.*, *12*, 101–112, 1995.

Kalnay, E., et al., The NMC/NCAR 40-Year Reanalysis Project, *Bull. Am. Meteorol. Soc.*, *77*, 437–471, 1996.

Kayano, M. T., Principal modes of the total ozone on the Southern Oscillation timescale and related temperature variations, *J. Geophys. Res.*, *102*, 25,797–25,806, 1997.

Marquardt, C., Die tropische QBO und dynamische prozesse in der stratosphere, Ph.D. dissertation, Freie Univ., Berlin, 1997.

Marquardt, C., and B. Naujokat, An update of the equatorial QBO and its variability, paper presented at 1st SPARC Gen. Assemb., Melbourne, Australia, *WMO/TD-No. 814*, Vol.1, 87–90, 1997.

McElroy, M. B., S. C. Wofsy, J. E. Penner, and J. C. McConnell, Atmospheric ozone: Possible impact of stratospheric aviation, *J. Atmos. Sci.*, *31*, 287–303, 1974.

McPeters, R., et al., Nimbus-7 Total Ozone Mapping Spectrometer (TOMS) data products user's guide, NASA Tech. Rep., 1996.

Naujokat, B., An update of the observed quasi-biennial oscillation of the stratospheric winds over the tropics, *J. Atmos. Sci.*, *43*, 1873–1877, 1986.

Plumb, R. A., and R. C. Bell, A model of the quasi-biennial oscillation on an equatorial beta-plane, *Q. J. R. Meteorol. Soc.*, *108*, 335–352, 1982.

Preisendorfer, R. W., *Principal Component Analysis in Meteorology and Oceanography*, 1st ed., 425 pp., Elsevier Sci., New York, 1988.

Press, W., S. Teukolsky, W. Vetterling, and B. Flannery, *Numerical Recipes in Fortran 77: The Art of Scientific Computing*, 2nd ed., 933 pp., Cambridge Univ. Press, New York, 1992.

Salby, M. L., and P. F. Callaghan, Fluctuations of total ozone and their relationship to stratospheric air motions, *J. Geophys. Res.*, *98*, 2715–2727, 1993.

Salby, M. L., and P. F. Callaghan, Connection between the solar cycle and the QBO: The missing link, *J. Clim.*, *13*, 2652–2662, 2000.

Shindell, D., D. Rind, N. Balachandran, J. Lean, and P. Lonergan, Solar cycle variability, ozone, and climate, *Science*, *284*, 305–308, 1999.

Shiotani, M., Annual, quasi-biennial, and El Niño-Southern Oscillation (ENSO) time-scale variations in equatorial total ozone, *J. Geophys. Res.*, *97*, 7625–7633, 1992.

Stephenson, D. B., and J. F. Royer, Low-frequency variability of total ozone mapping spectrometer and general-circulation model total ozone stationary waves associated with the El-Niño Southern Oscillation for the period 1979–1988, *J. Geophys. Res.*, *100*, 7337–7346, 1995.

Tung, K. K., and H. Yang, Global QBO in circulation and ozone: Part I. Reexamination of observational evidence, *J. Atmos. Sci.*, *51*, 2699–2707, 1994a.

Tung, K. K., and H. Yang, Global QBO in circulation and ozone. Part II: A simple mechanistic model, *J. Atmos. Sc.*, *51*, 2708–2721, 1994b.

World Meteorological Organization (WMO), Scientific Assessment of Ozone Depletion: 1998, *WMO Report No. 44*, Geneva, Switzerland, 1999.

C. D. Camp, Department of Applied and Computational Mathematics, California Institute of Technology, 1200 East California Boulevard, MS 150-21, Pasadena, CA 91125, USA. (cdc@gps.caltech.edu)

M. S. Roulston, Pembroke College, Cambridge CB2 1RF, UK.

Y. L. Yung, Division of Geological and Planetary Sciences, California Institute of Technology, 1200 East California Boulevard, MS 170-25, Pasadena, CA 91125, USA.